Coupling ferroelectric polarization and anisotropic charge migration for enhanced CO_2 photoreduction

Hongjian Yu [a], Hongwei Huang [a,*], Ali H. Reshak [b,c,d], Sushil Auluck [e], Lizhen Liu [a], Tianyi Ma [f,*], Yihe Zhang [a,*]

[a] Beijing Key Laboratory of Materials Utilization of Nonmetallic Minerals and Solid Wastes, National Laboratory of Mineral Materials, School of Materials Science and Technology, China University of Geosciences, Beijing, 100083, China
[b] University of Basrah, College of Science, Physics Department, Basrah, Iraq
[c] Department of Instrumentation and Control Engineering, Faculty of Mechanical Engineering, CTU in Prague, Technicka 4, Prague 6 166 07, Czech Republic
[d] Center of Excellence Geopolymer and Green Technology, School of Material Engineering, University Malaysia Perlis, 01007 Kangar, Perlis, Malaysia
[e] Council of Scientific and Industrial Research-National Physical Laboratory Dr. K S Krishnan Marg, New Delhi 110012, India
[f] School of Environmental & Life Sciences, The University of Newcastle (UON), Callaghan, NSW 2308 Australia

ARTICLE INFO

ABSTRACT

CO_2 photoreduction into solar fuels is promising for generating renewable energy. Herein, $SrBi_2Nb_2O_9$ nanosheets are prepared as high-performance photocatalysts for CO_2 reduction, highlighting superiority of ferroelectric polarization and anisotropic charge migration. Ferroelectric polarization within $SrBi_2Nb_2O_9$ nanosheets provides an in-built electric field, which greatly facilitates the bulk charge separation. Also, the photogenerated electrons and holes migrate separately to the NbO_6 octahedral layers and within the ab-plane in the Bi_2O_2 layers, achieving efficient anisotropic charge migration. Without co-catalyst or sacrificial agent, $SrBi_2Nb_2O_9$ nanosheets show outstanding CO_2 reduction activity in producing CH_4. The ferroelectric polarization is further enhanced by electric poling and annealing post-treatments. The electrically poled $SrBi_2Nb_2O_9$ shows a high CH_4 evolution rate of 25.91 $\mu mol\ g^{-1}\ h^{-1}$ with an AQE of 1.96 % at 365 nm, exceeding most of state-of-the-art photocatalysts reported to date. This work paves an avenue for development of highly efficient photocatalysts and beyond by tuning the ferroelectricity and electronic structure.

1. Introduction

Anthropogenic emission of CO_2 derived from the continuous consumption of fossil fuels seriously hinders the sustainable development of society and threatened human survival environment. Solar energy conversion of CO_2 into useful carbon-containing fuels serving as an appealing alternative has aroused tremendous interests [1–3]. However, the low photocatalytic CO_2 conversion efficiency is far from being sufficient for potential applications. Thus it is urgently required to explore high-performance photocatalysts [4–6]. In addition to possessing a favorable electronic structure that can offer strong photoreduction driving force, a robust photocatalyst must favor efficient separation of photo-excited electrons and holes to suppress their rapid recombination [7].

Establishing built-in electric field has been regarded as an efficacious strategy that is capable of furnishing a driving force to accelerate

photogenerated charge migration along different directions [8–11]. Particularly, incorporation of polarization electric field has lately shown huge potential in consumedly facilitating the charge separation across the bulk materials of polar $BiOIO_3$, [12] $Bi_4V_2O_{11}$, [13] Bi_4NbO_8X (X = Cl, Br), [14] $BiTiO_3$ [9] and $SrTiO_3$, [15] thereby promoting their photo- or piezo-catalytic oxidative ability. For ferroelectrics, there exists spontaneous polarization stemmed from the displacement of the center of the positive and negative charges in the unit cell, which can induce polarized charges (C+) and (C-) on the opposite surfaces. Thus, ferroelectric materials can be employed as effective co-catalysts to enhance interfacial electron/hole transport of catalysts through polarization-induced electric field. Nevertheless, few of them have been reported to be directly used as photocatalysts, especially for the harsh photo-reduction reaction, such as CO_2 reduction [16]. $SrBi_2Nb_2O_9$ is a typical representative of layered bismuth oxide perovskite with good piezoelectric and ferroelectric properties, as well as negative conduction

---

band (CB) position [17]; it shows benign photocatalytic performance for organism degradation and water splitting [17,18]. At present, the synthesis of $SrBi_2Nb_2O_9$ powder mainly adopts traditional solid-state reaction, molten salt method and sol-gel process [17,19,20]. The large-size grains derived from these approaches suffer from insufficient reactive sites for CO_2 adsorption, which significantly depresses the photoreactivity. Therefore, it is highly challenging and promising to explore the photocatalytic CO_2 performance of nanoscaled ferroelectric semiconductors (i.e. nanostructured $SrBi_2Nb_2O_9$) and to elucidate the relationship between ferroelectricity and photogenerated charge separation efficiency.

Herein, we report the successful preparation of $SrBi_2Nb_2O_9$ nanosheets with excellent ferroelectric properties by a one-pot hydrothermal route with assistance of sodium hydroxide as the mineralizer. Density Functional Theory (DFT) calculations reveal that the photogenerated electrons transfer to NbO_6 octahedral layers and migrate along *c* axis, while the holes are mostly confined within the *ab*-plane in the Bi_2O_2 layers, realizing efficient anisotropic charge migration. The polarization-induced electric field enhancement for $SrBi_2Nb_2O_9$ nanosheets is demonstrated to substantially promote charge separation. Annealing post-treatment and electric poling as deep polarization-enhancement strategies are applied to further foster the ferroelectricity of $SrBi_2Nb_2O_9$ nanosheets. Impressively, the as-synthesized catalyst with the strongest polarization casts a ~81 times enhancement in CH_4 evolution compared with the bulk $SrBi_2Nb_2O_9$ derived from solid-state reaction, with a high rate of 25.91 μmol g^{-1} h^{-1} and high electron consumption selectivity, exceeding most of reported established photocatalysts; this outcome highlights the vital roles of excellent electronic structure and ferroelectricity in promoting photocatalytic CO_2 reduction reactivity.

2. Experimental

2.1. Synthesis

All of the reagents used in this work are analytical grade and used as received without further purification. The $SrBi_2Nb_2O_9$ are synthesized with $Bi_2(SO_4)_3$ as bismuth source (SBN-HR) according to the following process : First, 1 mmol $SrCl_2$ $6\cdot H_2O$ (Sinopharm) and 1 mmol $Bi_2(SO_4)_3$ (Sinopharm) are dissolved in dilute nitric acid to obtain solution A. Meanwhile, a certain amount of NaOH (Sinopharm) is dissolved in deionized water and defined as mineralizer solution B. Then, the solution B is added into the solution A to form a homogeneous mixed solution C and keep the mineralizer concentration as 4 mol/L. After that, 1 mmol Nb_2O_5 (Sinopharm) is added into the solution C and stirred for 30 min. Then the suspension is transfer to 50 ml Teflon-lined autoclave and heated under 220 °C for 24 h. The white products are washed with deionized water for several times and dried at 60 °C for 12 h in a vacuum drying oven. The $SrBi_2Nb_2O_9$ are synthesized with $Bi(NO_3)3\cdot 5H_2O$ (Sinopharm) (SBN-HR-1) and $BiCl_3$ (Sinopharm) (SBN-HR-2) as bismuth source are obtained in the same way (Fig. S1).

Annealing treatment: The SBN-HR nanosheets are heated in a muffle furnace at 400 °C (Annealed at 400 °C) and 700 °C (Annealed at 700 °C) in air for 2 h, respectively (Fig. S1).

Poling process : First of all, the pellets prepared by ferroelectric $SrBi_2Nb_2O_9$ nanosheets are coated with silver paste on both the surfaces. Then, the pellets are directly poled with different voltage (5, 10, 20, 30 kV/cm) in a silicone oil bath for 30 min. Finally, silver coating from the surfaces is removed by sandpaper to obtain poled samples labelled as SBN-HR-X kV/cm (X = 5, 10, 20, 30).

The $SrBi_2Nb_2O_9$ is prepared by solid state reaction (SBN-SSR) according to the following process : The starting materials of $SrCO_3$ (Sinopharm), Bi_2O_3 (Sinopharm) and Nb_2O_5 are mixed evenly according to a certain stoichiometry. Then, the mixture is heated at 850 °C for 20 h. BiOBr is obtained by a simple hydrolysis method through mixing the Bi $(NO_3)3\cdot 5H_2O$ (1 mM) solution and KBr (1 mM) solution, and C_3N_4 is

prepared by calcination of melamine at 550 °C for 2 h.

2.2. Characterization

The phase structure of obtained samples are researched by X-ray diffraction (Bruker AXS, Germany) with Cu Kα radiation (λ =1.5418 Å). The microstructure and morphology of as-prepared materials are analyzed by a scanning electron microscopy (SEM, S-4800 Hitachi, Japan). Transmission electron microscopy (TEM) images and High-resolution transmission electron microscopy (HRTEM) images are acquired by a Tecnai F20 electron microscopy. The optical properties of the samples are obtained by a UV–vis spectrometer (Cary 5000 Varian, America) using $BaSO_4$ as the reference. The X-ray photoelectron spectroscopy (XPS, ESCALAB 250 Xi ThermoFisher, UK) is used to get the chemical compositions of the as-synthesized samples. AFM are characterized using Oxford MFP-3D AFM (Oxford MFP-3D, UK) under electric force microscope pattern (EFM). The ferroelectric properties are measured by a ferroelectric tester (aixACCT Systems GmbH, Aachen, Germany). The photoluminescence emission (PL) is measured by a fluorescence spectrophotometer (F-4600 Hitachi, Japan).

2.3. Photocatalytic CO_2 reduction test

The products of reduction CO_2 are carried out in a gas-solid reaction system with a Labsolar-III AG closed circulation system (Beijing Perfect light Technology Co., Ltd., China). 0.2 g photocatalyst is evenly dispersed on the upper shelf of the reactor, and 1.3 g $NaHCO_3$ were uniformly placed at the bottom of the reactor followed by thorough pumping vacuum. Subsequently, 5 ml H_2SO_4 (4 M) is injected into the vacuum reactor to react with $NaHCO_3$ to get 1 atm CO_2 gas. A 300 W Xe lamp using an AM1.5 G filter with the intensity of 100 mW cm^{-2} was used as light source to irradiate the reactor under photoreaction temperature keeping at 20 ℃. After, 1 ml of gas is taken for subsequent qualitative analysis by GC9790II gas chromatography (Zhejiang Fuli Analytical Instrument Co.) with a thermal conductivity detector (Fig. S2). 365 nm monochromatic light is used to test the apparent quantum efficiency (AQE) by the following equation:

$$AQE(\%) = \frac{N_{Solar\,fuels}}{N_p}$$

$$= \frac{2 \times number\,of\,CO\,molecules + 8 \times number\,of\,CH_4\,molecules}{The\,number\,of\,incident\,photos} \times 100\%$$

$$= \frac{N_a \times (2M_{CO} + 8M_{CH_4})}{\frac{PSt\lambda}{hc}}$$

Where, $N_a = 6.02 \times 10^{23}$ mol^{-1}, P = 14.1 mW/cm^2, S = 3.14 cm^2, t = 3600 s, λ = 365 × 10^{-9} m, h = 6.626 × 10^{-34} J s, and c = 3 × 10^8 m/s.

2.4. Photoelectrochemical test

Photocurrent and electrochemical impedance spectroscopy (EIS) measurements of samples are conducted in a three-electrode system with on an electrochemical system (CHI-660E, Shanghai, China). In this system, a saturated calomel electrode (SCE) is utilized as the reference electrode and platinum wires are the counter electrode, and the electrolyte solution is 0.1 M Na_2SO_4 solution. The sample films are coated on indium-tin oxide (ITO) glass as the working electrode. A 300 W xenon lamp is used as the visible light source. There is no applied voltage between the electrodes. And the measurements are conducted at room temperature.

2.5. Density functional theory (DFT) calculation

To reveal the crystal structure, density of states and electronic band

structure of SrBi$_2$Nb$_2$O$_9$, DFT calculation is analyzed by utilizing CASETP code implemented planewave method and Perdew-Burke-Ernzerhof function. A discrete k mesh along the high-symmetry directions of band structures is calculated by VASP to obtain the effective mass along the different directions. The carrier effective mass is evaluated from the second derivative of the highest point of the VB band and the lowest point of the CB band according to E = ℏ^{2}k^2/2m$_e$m*, where me denotes the free electron mass (9.1 × 10^{-19} kg) [21].

3. Results and discussion

3.1. Materials synthesis and characterization

SrBi$_2$Nb$_2$O$_9$ possesses a layered crystal structure constructed by alternating [Bi$_2$O$_2$] layers and double-perovskite [Nb$_2$O$_7$] slabs along the *c* axis, with Sr atoms residing in the tunnels of [Nb$_2$O$_7$] slabs (Fig. 1a). SrBi$_2$Nb$_2$O$_9$ crystallizes in an orthorhombic space group *A2$_1$am* with lattice parameters of *a* = 5.58 Å, *b* = 5.57 Å and *c* =25.36 Å [20],

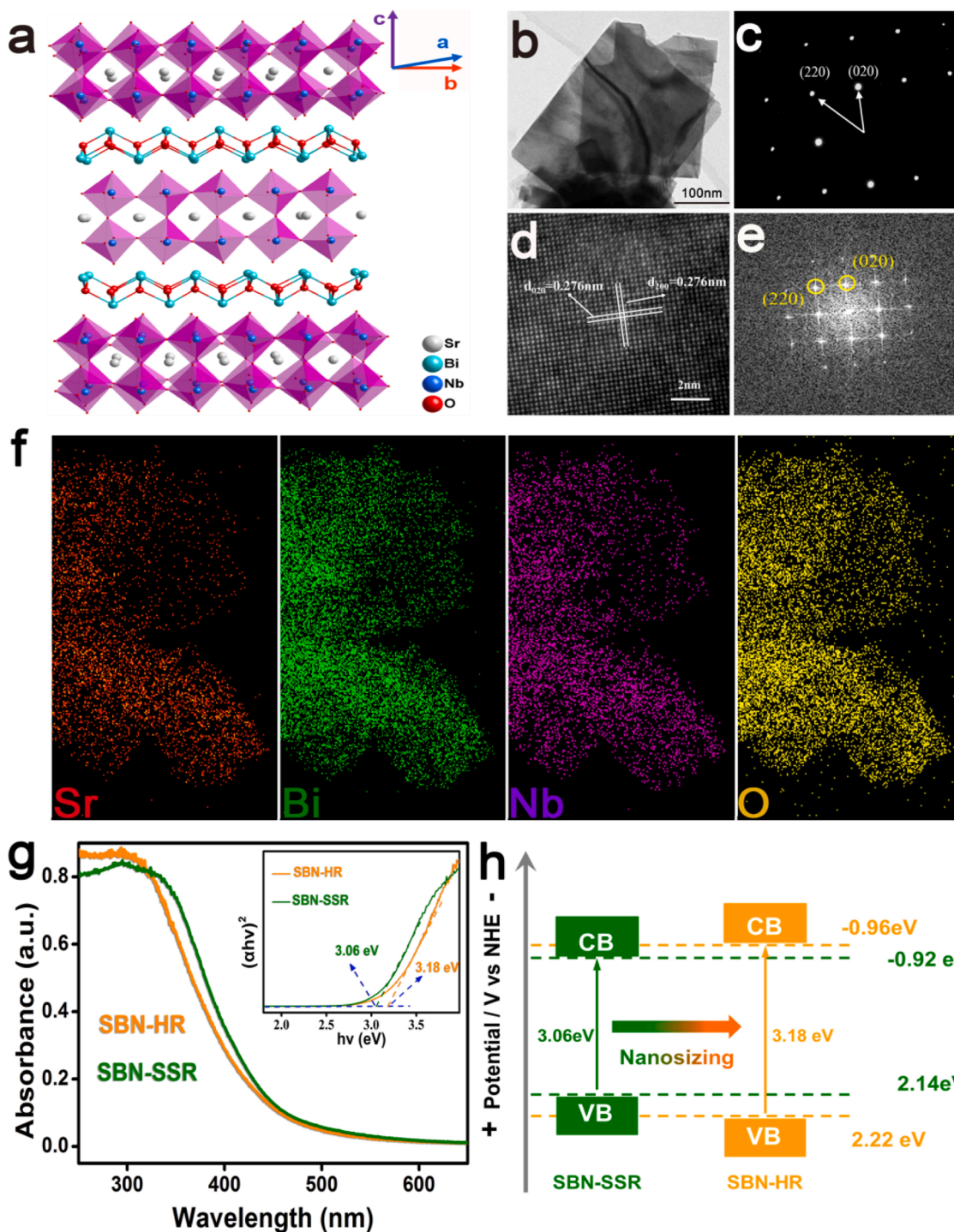**Fig. 1.** a) Crystal structure of SrBi$_2$Nb$_2$O$_9$. b) TEM image, c) SAED pattern, d) HRTEM image and e) the corresponding FFT pattern of SBN-HR. f) EDX elemental mappings of Sr, Bi, Nb and O of the SBN-HR. g) UV–vis diffuse reflectance spectra (DRS) and band gap (inset) and h) band structure diagrams of SBN-SSR and SBN-HR.

which implys a ferroelectric nature. Herein, $SrBi_2Nb_2O_9$ nanosheets (denoted as SBN-HR) are for the first time prepared by introducing NaOH as the mineralizer during the hydrothermal reaction. For comparison, $SrBi_2Nb_2O_9$ is also synthesized by the traditional high-temperature solid-state reaction (denoted as SBN-SSR). Their XRD patterns well match the diffraction pattern of orthorhombic phase $SrBi_2Nb_2O_9$ (PDF#49-0607) (Fig. S3). Obviously, the evidently broadened diffraction peaks of SBN-HR grain reveal the nanosizing effect. X-ray photoelectron spectroscopy (XPS) (Figs. S4 and S5) demonstrates the presence of Sr^{2+}, Bi^{3+}, Nb^{5+} and O^{2-} in SBN-HR and SBN-SSR with expected stoichiometry. Compared with that of SBN-HR, both the binding energy of Nb 3d and Bi 4f in the XPS spectra of SBN-SSR exhibit an obvious shift of ~ 0.15 eV to lower binding energies (Table 1), which may be attributed to the formation of oxygen vacancies. Besides, the Sr 3d and O 1s XPS spectra of SBN-SSR also show the similar shift to the low energy.

Microstructure of the samples prepared by different methods is analyzed by the electron microscopic techniques. SBN-SSR shows irregular morphology with the particle size ranging from 0.5 to 2 μm (Fig. S6a), wherein the large particle size is due to agglomeration at high temperature. In sharp contrast, hydrothermally prepared SBN-HR consists of uniform nanosheets with thickness of 10−30 nm (Fig. S6b), consistent with the XRD result. The Brunauer-Emmett-Teller (BET) specific surface area (Fig. S7) of SBN-HR is 31.5 m^2/g, which is 4.4 times that of SBN-SSR (7.1 m^2/g). TEM image (Fig. 1b) confirms the nanosheet structure of SBN-HR with the planar size of 200−300 nm. Selected area electron diffraction (SAED) pattern reveals a regular and clear diffraction spot array, indicative of high crystallinity; this particular SAED pattern is assigned to the [001] zone-axis diffraction spots of orthorhombic $SrBi_2Nb_2O_9$ (Fig. 1c). HRTEM image shows two sets of perpendicular crystal lattices with an interplanar spacing of 0.276 nm (Fig. 1d), which are assigned to the (020) and (200) planes of $SrBi_2Nb_2O_9$. The fast Fourier transform (FFT) pattern (Fig. 1e) further confirms the SAED and the HRTEM observations. Thus, the dominantly exposed facet of SBN-HR is {001} facet, in accordance with the layered crystal structure feature of $SrBi_2Nb_2O_9$ along *c* axis. TEM energy dispersive X-ray (EDX) elemental mapping (Figs. 1f and S8) indicates the homogeneous distribution of Sr, Bi, Nb and O elements across SBN-HR nanosheets.

Optical energy band structure is the foundation to understand the photo-induced reduction and oxidation reaction of a photocatalyst. DFT calculation is conducted to resolve the electronic band structure of $SrBi_2Nb_2O_9$ (Fig. S9). The valence band maximum (VBM) and the conduction band minimum (CBM) are both located at the R point, indicating $SrBi_2Nb_2O_9$ as a direct-transition semiconductor with a theoretical bandgap of ~3 eV. UV/vis diffuse reflectance spectra (DRS) demonstrates that the absorption edges of SBN-SSR and SBN-HR are approximately 450 nm. SBN-HR displays a clear blue shift in absorption edge compared to SBN-SSR (Fig. 1g), which is consistent with the nanosheet morphology of SBN-HR [5]. The bandgap energies of SBN-SSR and SBN-HR, estimated from the plot of $(ah\upsilon)^{1/2}$ versus photon energy ($h\upsilon$), are 3.06 and 3.18 eV, respectively (inset of Fig. 1g). Mott-Schottky (M-S) method is employed to analyze the flat band (FB) energy potential, which are determined as -1.16 and -1.20 eV versus SCE for SBN-SSR and SBN-HR, respectively (Fig. S10). Since the CB position are situated near the flat band potential, it is easy to know that the CB position of SBN-HR is approximately -0.04 eV higher than that of SBN-SSR. By combining

UV/vis DRS results, it is concluded that SBN-HR has a more positive valence band (VB) position than SBN-SSR by 0.08 eV, as illustrated in the schematic band structure (Fig. 1h).

3.2. CO₂ photoreduction performance

The photocatalytic CO_2 reduction performance of the samples is measured in a gas-solid reaction system with illumination of simulated solar light (Fig. 2a–c). SBN-SSR shows an inferior CO_2 reduction activity with CH_4 and CO production rates of 0.32 and 0.37 μmol g^{-1} h^{-1}, respectively. In stark contrast, the CH_4 evolution rate of SBN-HR is 8.75 μmol g^{-1} h^{-1}, which is ~27.3 times that of SBN-SSR, while the CO production rate stays almost the same to that of SBN-SSR. It should be noted that the enhancement factor of catalytic activity far exceeds that of specific surface area (4.4 times). In order to exclude the possibility of influence from organic impurities on the surface of samples, Ar is purged into the reactor instead of CO_2 during the photoreaction, no CH_4 and CO are detected in the photocatalytic CO_2 reduction process (Figs. 2d and S11), When CO_2 is refilled in the above Ar-containing system, a large amount of CH_4 and trace of CO are detected again, as displayed by the GC–MS spectra (Fig. S12). For further verification, the corresponding possible oxidative product O_2 generated during the CO_2 reduction process is surveyed. As illustrated in Fig. S13, the production rate of O_2 to CH_4 in molar ratio is always kept at 2:1, which demonstrates that the redox reactions have actually occurred on $SrBi_2Nb_2O_9$ via photocatalysis, and CH_4 is the dominanting reductive product besides a trace amount of CO. No CH_4 and CO (Figs. 2d and S14) are detected in the dark or without photocatalysts, further confirming the vital role of SBN-HR. The unchanged XRD pattern, BET and UV–vis diffuse reflectance spectra after photoreaction and no obvious activity decay after four consecutive cycles reflect the high stability of SBN-HR (Figs. S15–S18).

For verifying the excellent photocatalytic activity of SBN-HR, several classic photocatalysts, such as P25 (commercial TiO_2), C_3N_4 and BiOBr, are employed as references. The detailed synthesis methods for control groups can be found in the experimental section. It is evident that SBN-HR far outperforms P25, C_3N_4 and BiOBr in terms of the production of CH_4 (Fig. 2c), though they possess comparable specific surface areas (Fig. S19). Besides, the $SrBi_2Nb_2O_9$ photocatalysts are also hydrothermally synthesized by using other bismuth-containing salts as the precursors ($Bi(NO_3)35$'H_2O and $BiCl_3$); the crystalline phase of corresponding products denoted as SBN-HR-1 and SBN-HR-2 is confirmed by their XRD patterns (Fig. S20). These nanosheets prepared by different precursors all display high photocatalytic CO_2 reduction performance for CH_4 production (Fig. S21).

To reveal the mechanism of the CO_2 conversion on SBN-HR, *in situ* FTIR experiments are carried out. The almost straight curves at 0 and 30 min exclude the influence of surface organic impurities on the detection of reduction products for SBN-HR (Fig. 2e). The strong peaks at around 2300 cm^{-1} are due to the asymmetric stretching of CO_2, suggesting that SBN-HR has good adsorption of CO_2 (Fig. S22) [22]. Under light irradiation with purging CO_2, the peaks at around 1300–1590 cm^{-1} and 1610–1900 cm^{-1} appear, and their intensities keep growing with prolonging irradiation time. Notably, the peaks at around 1335–1560 cm^{-1} and 1610–1750 cm^{-1} respectively belong to the bending vibration of CH—, the stretching vibration of C=O and the asymmetric stretching of O—CO=, which are attributed to the intermediate products, such as aldehydes, carboxylic acids, and bidentate carbonates [22,23]. CO_2 is constantly transformed into various intermediate species, such as CO_2^- (1701 cm^{-1}), b-CO_3^{2-} (1650 and 1365 cm^{-1}), m-CO_3^{2-} (1458, 1540 and 1557 cm^{-1}) and HCO_3^- (1425 and 1474 cm^{-1}), and the peaks at 1339 cm^{-1} and 2890–3010 cm^{-1} are attributed to the bending vibration and stretching vibration of CH— in CH_4 [3,24], strongly confirming the generation of methane. The possible electron/proton transport processes and their formation processes were speculated based on the amount of final products and the intermediate products (Fig. S23).

Table 1

Calculated effective masses of charge carriers $SrBi_2Nb_2O_9$ along different directions.

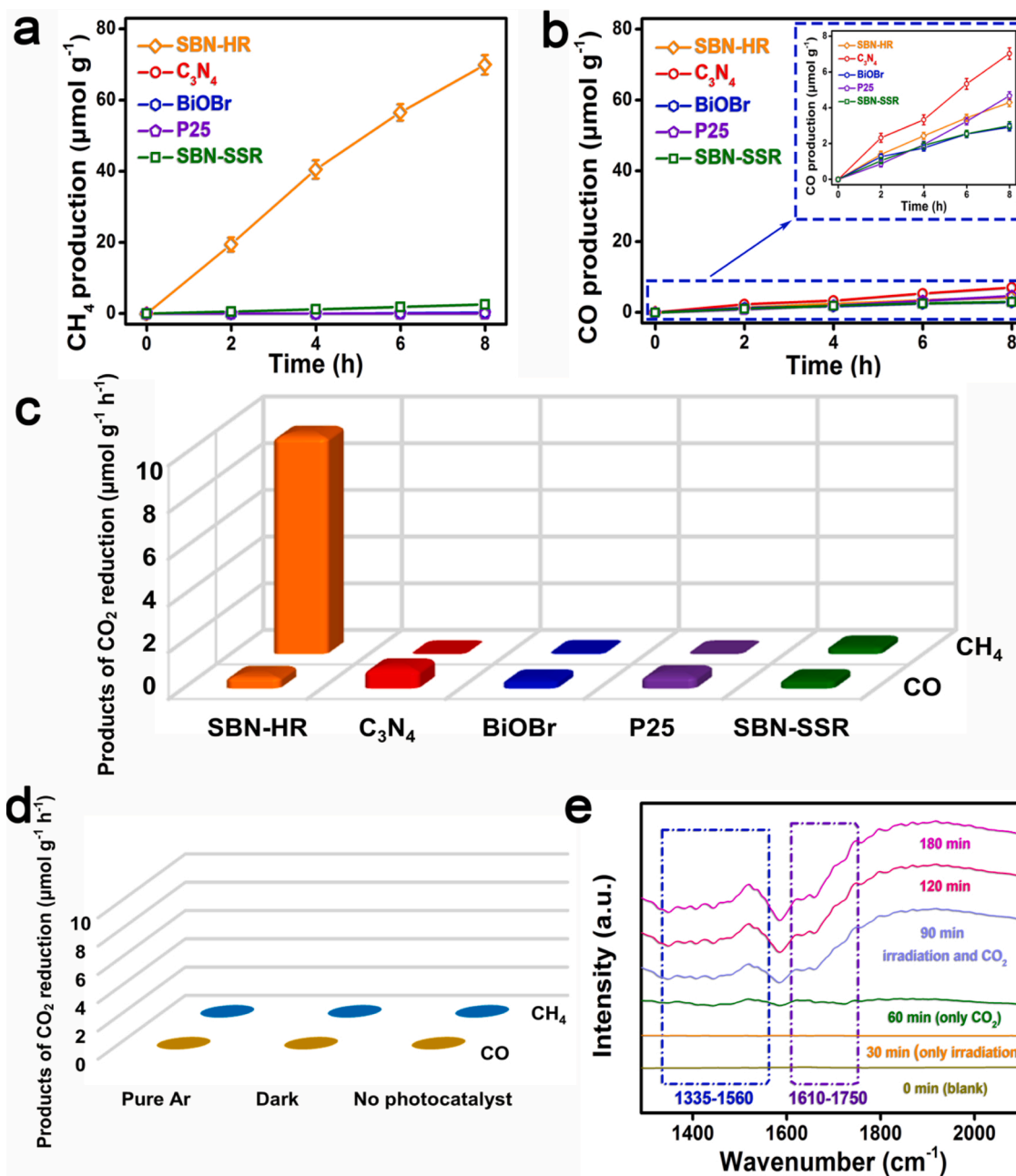| Direction	m_e^*/m_o	m_h^*/m_o	m_h^*/m_e
[0 1 0]	0.02	0.08	3.90
[1 0 0]	0.02	0.08	3.85
[0 0 1]	0.01	0.18	17.96

Fig. 2. a, b) CO and CH$_4$ production curves and c) corresponding production rates over SBN-HR, C$_3$N$_4$, BiOBr, P25 and SBN-SSR under simulated solar light. d) Photocatalytic CO$_2$ reduction rates with purging highly-pure Ar instead of CO$_2$, in the darkness and without photocatalyst. e) *in situ* FTIR spectra of SBN-HR under different conditions.

3.3. Band structures and anisotropic charge migration

To understand the high photocatalytic CO$_2$ activity of SrBi$_2$Nb$_2$O$_9$, the electronic band composition is analyzed by calculating the densities of states of SrBi$_2$Nb$_2$O$_9$ (Figs. 3a, b and S24). The top of VB is mainly composed of hybridized Bi 6 s and O 2p orbitals, and the bottom of CB dominantly originates from the Nb 4d orbital. It illustrates that the photogenerated hole will migrate to the Bi$_2$O$_2$ layers, while the photogenerated electrons transfer to the NbO$_6$ octahedral layers. Owing to that the photogenerated electrons and holes are respectively converged in different structural domains, the spatial separation of photogenerated charge carriers is achieved in the unit cell of SrBi$_2$Nb$_2$O$_9$. Then, the effective mass of charge carriers along different directions is calculated to provide in-depth insight into the high photocatalytic CO$_2$ activity (Table 1). It is demonstrated that the hole has a relatively large effective

mass along the [001] direction, while the effective mass of electron along this direction is small. The relative ratio (D) of the effective mass of electrons (m*$_e$) and holes (m*$_h$) is defined to evaluate the recombination rate in Equation 1 [25]. A great difference between their effective masses is beneficial to improve the separation efficiency [1].

$$D = m^*_h/m^*_e \qquad\qquad (1)$$

It is noteworthy that a very high D value (~18 times) is found along the [001] direction, which indicates a significantly depressed recombination of photogenerated electrons and holes. In another word, the electrons move much faster than holes along *c* direction, which migrate to the NbO$_6$ octahedral layers from the Bi$_2$O$_2$ layers and then quickly participate in the redox reaction. However, the holes are mostly confined within the *ab*-plane in the Bi$_2$O$_2$ layers. Namely, the
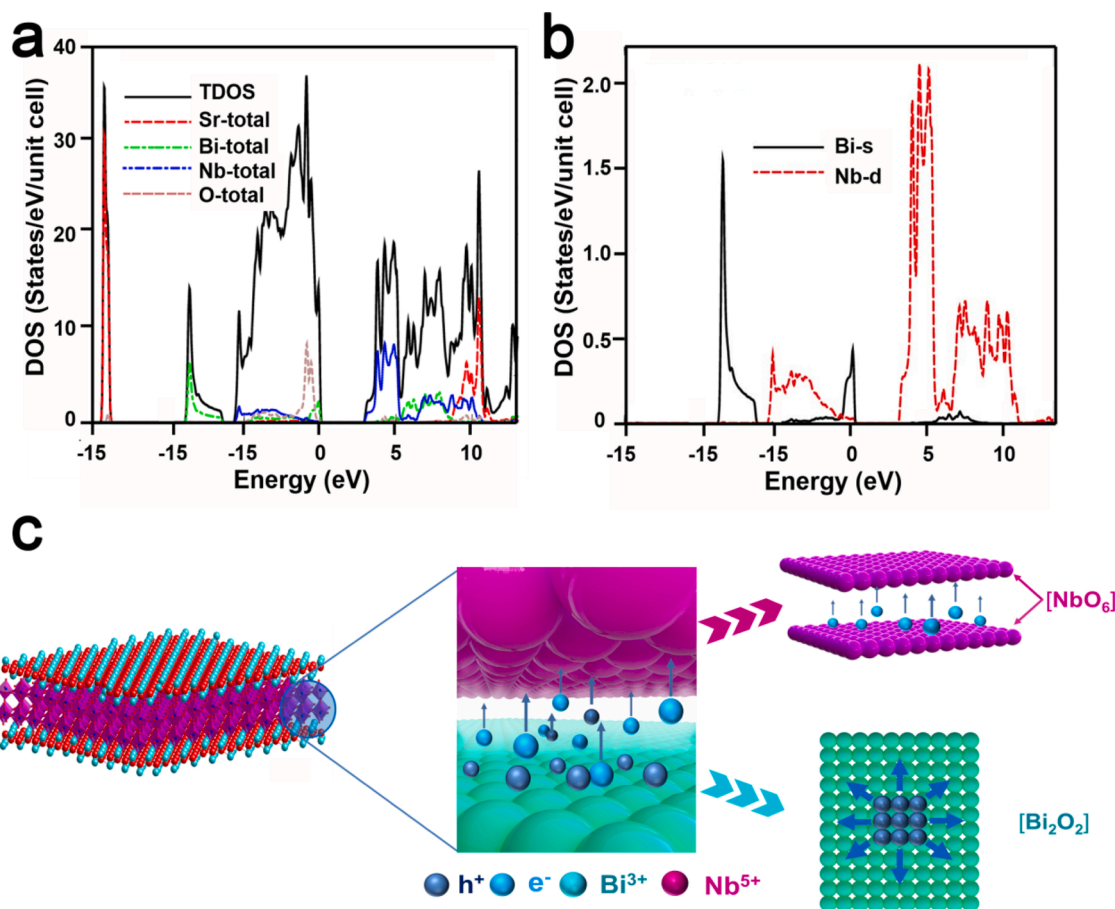
Fig. 3. a, b) Density of states (DOS) of $SrBi_2Nb_2O_9$. c) Schematic diagram for separation and migration of photogenerated electrons and holes along different directions in the units.

photogenerated electrons and holes not only are separated and accumulated in different structural groups, but also achieve efficient anisotropic charge migration, which consumedly promote the photocatalytic activity of $SrBi_2Nb_2O_9$ nanosheets. Particularly, the nanosheet structure of $SrBi_2Nb_2O_9$ with predominantly exposed {001} facet maximizes the advantage of anisotropic charge migration via greatly shortening the electron migration pathway, benefiting the subsequent photocatalytic reactions.

3.4. Polarization-induced electric field in promoting the charge separation

Inspired by the much larger enhancement level (27.3 times) of catalytic activity than that of specific surface area (4.4 times) of SBN-SSR compared to SBN-HR, charge separation efficiency as a crucial factor affecting the photocatalytic activity is surveyed. Surface photovoltage (SPV) spectroscopy is an effective and convincing mean to reveal information of the charge separation and recombination of photoinduced electrons and holes, in which magnitude of the SPV signal reflects the charge separation degree [26]. Compared with SBN-SSR, SBN-HR displays an evidently magnified signal in the range of $280-420$ nm, in which the intensity increases by a factor of 5 (Fig. 4a). It provides a reliable evidence that SBN-HR shows higher charge separation efficiency than SBN-SSR.

Since polarization-induced electric field largely affects the charge separation of a ferroelectric, their ferroelectricity properties are investigated to probe the origin for the charge separation difference between SBN-SSR and SBN-HR. From the hysteresis $P–E$ loops (Fig. 4b), SBN-HR displays remarkably higher saturation polarization, remnant polarization and coercive field, suggesting its much stronger polarization-

induced electric field. The nonstandard hysteresis $P–E$ loops of SBN-HR are dominated by the leakage current and lower density. The amplitude and phase maps of the SBN-HR (Figs. S25–S27) also confirm the excellent piezoelectric properties of SBN-HR. Piezoresponse force microscopy (PFM) discloses the domain structure of the SBN-HR, which exhibits the dark and bright regions, illustrating the negatively and positively polarized domains, respectively (Fig. 4c and d). Surface charge image shows that the surface of SBN-HR has different charges (Fig. 4e and f), which indicates that polarized electric field is formed between dark and bright regions. In spite of the advantages in morphology, specific surface area, anisotropic charge migration and energy band structure related to the photocatalytic performance of the catalyst, these results strongly demonstrate the existence of stronger polarization-induced electric field in $SrBi_2Nb_2O_9$, which plays an important role in inducing superior charge separation efficiency.

To corroborate the critical role of the polarization-induced electric field in promoting the charge separation and photocatalytic performance, $SrBi_2Nb_2O_9$ nanosheets are annealed at different temperatures (400 and 700 °C), as it is reported that annealing may has a large impact on the ferroelectricity [27–29]. The photoabsorption and band energy edge of as-prepared SBN-HR nanosheets and the annealed samples at different temperatures show no visible difference (Figs. S28–S30). With the increase of annealing temperature, the nanosheets become larger and thicker with sharper and stronger XRD diffraction peaks (Figs. S31 and S32), which indicates that high annealing temperature contributes to the crystal growth and the crystallinity improvement of samples. Accordingly, the specific surface area decreases with the increase of annealing temperature (Fig. S33). It is interesting to observe that the two annealed samples exhibit enhanced photocatalytic CO_2 reduction
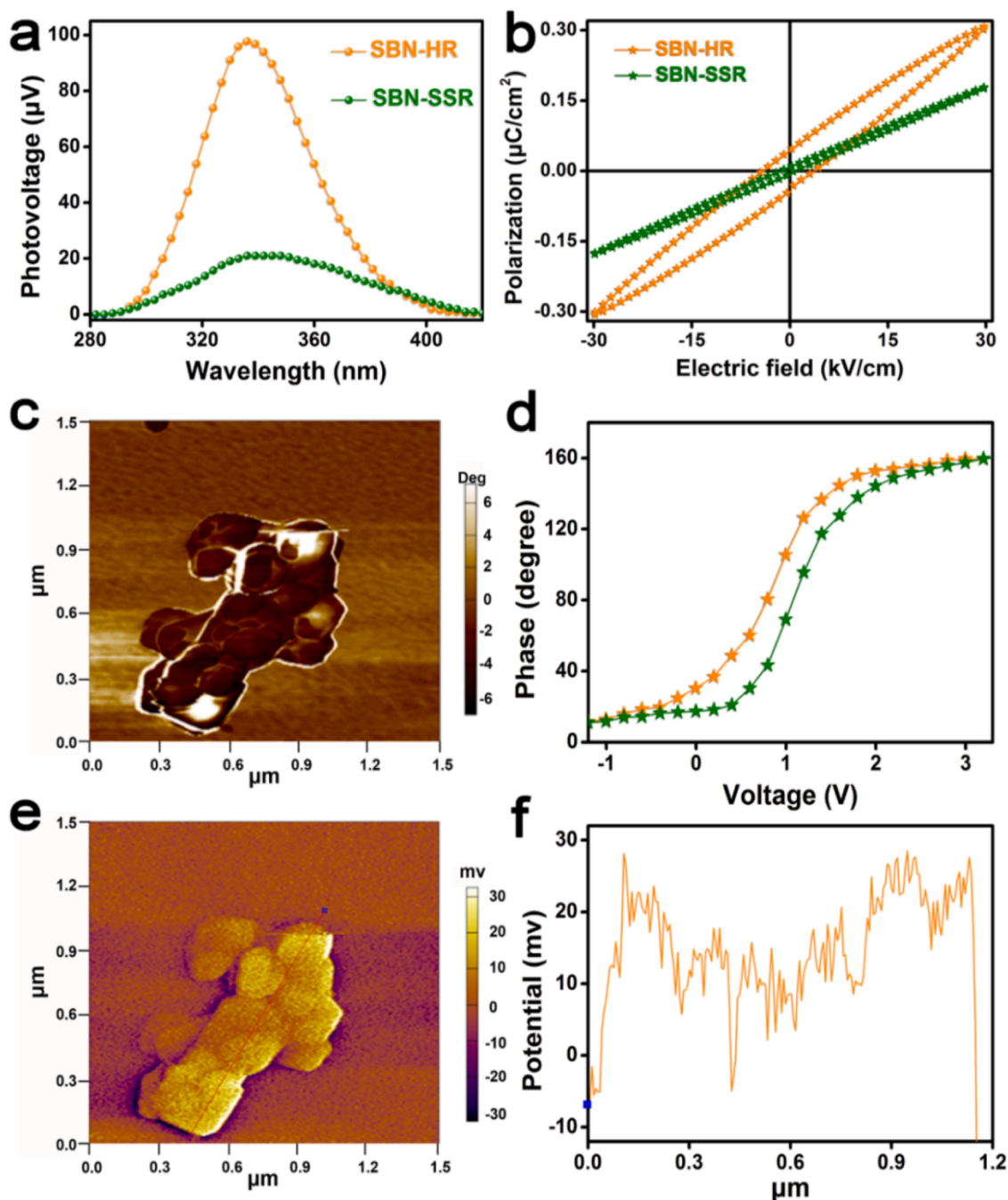
Fig. 4. a) SPV spectra and b) polarization-electric feld hysteresis loops of the SBN-HR and SBN-SSR. c) The standard ferroelectric phase image and d) ferroelectric phase curve of SBN-HR. e) Surface charge and f) corresponding charge difference profile of SBN-HR.

performance for both CH_4 and CO production in comparison to the un-annealed $SrBi_2Nb_2O_9$ (Fig. 5a–c). Particularly, the $SrBi_2Nb_2O_9$ nanosheets annealed at 400 °C exhibits the highest CH_4 yield with an evolution rate of 18.25 μmol g^{-1} h^{-1}, which is 57 times that of bulk $SrBi_2Nb_2O_9$. Also, the O_2 yielding amount shows the same order to that of CH_4 (Fig. 5c). It should be noted that annealing treatment effectively eliminates the organic impurities adsorbed on the catalysts, which further corroborates the high CO_2 reduction performance originating exclusively from the photocatalytic process [30].

In order to better reveal the relationship between charge separation efficiency and ferroelectricity, the measurements on surface photo-voltage (SPV) spectroscopy, photocurrent and electrochemical imped-ance spectroscopy (EIS) Nyquist plots of as-prepared SBN-HR nanosheets and the annealed samples at different temperatures are

conducted. As shown in Figs. 5d and S34 and S35, the SBN-HR nano-sheets annealed at 400 °C display the strongest photovoltage response, highest current density and smallest arc radius followed by the one annealed at 700 °C and the untreated SBN-HR, indicating the charge separation efficiency and interfacial resistance are improved by the annealing post-treatment. Apart from enhanced charge separation, SBN-HR annealed at 400 °C shows more alkaline sites for stronger adsorption of CO_2 than SBN-HR (Fig. S36).

The hysteresis loops of SBN-HR annealed at different temperatures reveal that the ferroelectric polarization magnitude follows the order of SBN-HR annealed at 400 °C > SBN-HR annealed at 700 °C > SBN-HR (Fig. 5e). The ferroelectricity tops at SBN-HR annealed at 400 °C instead of the one annealed at 700 °C. It can be rationalized as follows. As the grains of SBN-HR grow up with the increase of annealing
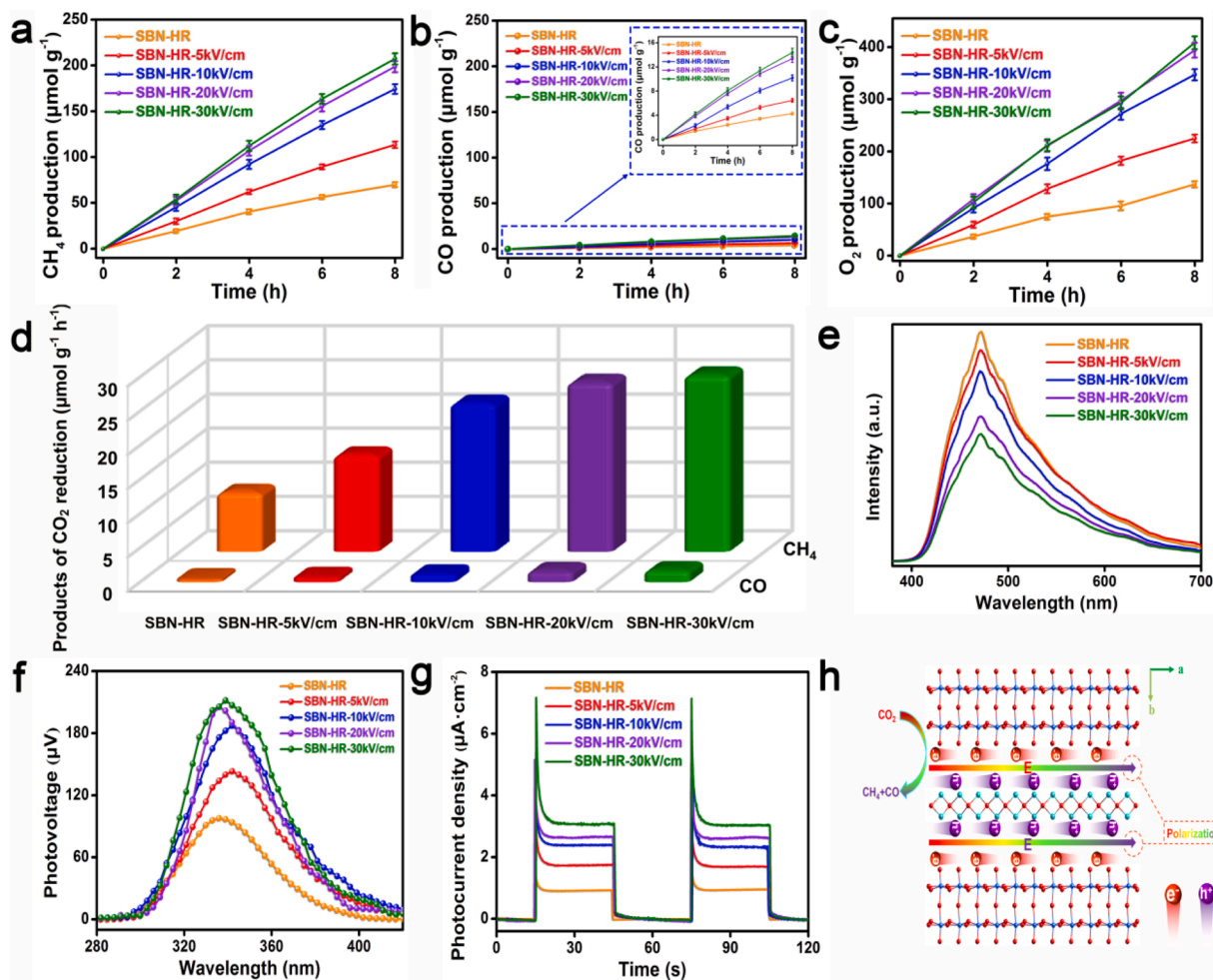
Fig. 5. a, b) Photocatalytic CH_4 and CO production curves and c) the corresponding products rates over the as-prepared SBN-HR, SBN-HR annealed at 400 °C and SBN-HR annealed at 700 °C under simulated solar light. d) SPV spectra and e) polarization-electric feld hysteresis loops of as-prepared SBN-HR, SBN-HR annealed at 400℃ and SBN-HR annealed at 700℃.

temperature, the ferroelectricity is enhanced within a certain range [27, 28], owing to the reduced volume fraction of the grain boundaries and the easier reorientation of the domains [27,31]. When SBN-HR is annealed at high temperature (e.g. 700 °C), the evaporation of Bi from the sample's surface results in abundant nonstoichiometric structural defects, which decreases the ferroelectric property [28,32]. Significantly, the ferroelectric polarization magnitude order of these samples accords well with the above results of charge separation efficiency and photocatalytic CO_2 reduction activity, which provides further proofs that the enhancement on polarization-induced electric field greatly facilitates the charge separation of $SrBi_2Nb_2O_9$, subsequently promoting the photocatalytic CO_2 reduction performance.

Though annealed samples have no obvious difference in specific surface area and band structure, the change of crystallinity may show an influence on the photocatalytic performance. To further clarify the relationship between charge separation efficiency and polarization-induced electric field, the electric poling is conducted on $SrBi_2Nb_2O_9$ nanosheets with an external electric field of 5, 10, 20 and 30 kV/cm. The poled samples under different electric fields show almost unchanged photoabsorption, band energy edge, crystallinity and specific surface area in comparison with those key parameters of SBN-HR (Figs. S37–S42). Significantly, all the obtained samples after different electric fields poling on SBN-HR nanosheets show greatly improved CH_4 and CO production (Fig. 6a, b and d). The CH_4 evolution rate of SBN-HR-30 kV/cm is further increased to 25.91 μmol g^{-1} h^{-1}, which is ~81 times that of bulk $SrBi_2Nb_2O_9$. It also outperforms most of reported bismuth-

based photocatalysts and established photocatalysts (see detailed comparison in Table S2), such as BiOI (1.78 μmol g^{-1} h^{-1}) [4], $Bi_4O_5Br_2$ (2.04 μmol g^{-1} h^{-1}) [33] and Bi_2WO_6 (1.10 μmol g^{-1} h^{-1}) [30]. The production rate of O_2 to (CO, CH_4) also accords the ratio of their transported electrons in the redox reactions (Fig. 6c), demonstrating that the photocatalytic redox reactions have actually occurred on $SrBi_2Nb_2O_9$ under simulated solar light. No detectable H_2 and other liquid carbon-containing products suggest that SBN-HR-30 kV/cm possesses dominant electron consumption selectivity for CH_4 production. No CH_4 and CO are detected under Ar in the dark or without photocatalysts (Fig. S43), further confirming that it is SBN-HR-30 kV/cm initiating the reaction. In addition, to rule out the influence of silver paste on the poled catalysts in the poling process, XPS is conducted. There are no Ag and other residues in the catalyst, excluding potential catalytic effects of alien species (Fig. S44). Notably, the almost unchanged photocatalytic CO_2 reduction performance of SBN-HR-30 kV/cm after a prolonged testing period of half a year reflects its highly stable photocatalytic activity (Fig. S45). Besides, the apparent quantum efficiency (AQE) of the SBN-HR-30 kV/cm is determined, which reaches 1.96 % at 365 nm. This high AQE confirms that as-prepared $SrBi_2Nb_2O_9$ nanosheets can efficiently convert solar energy into solar fuel.

Photoluminescence spectra can reflect the recombination degree of photogenerated electrons and holes, and the high emission intensity indicates a large charge recombination rate. Evidently, the four poled SBN-HR samples show decreased intensity of emission peaks in
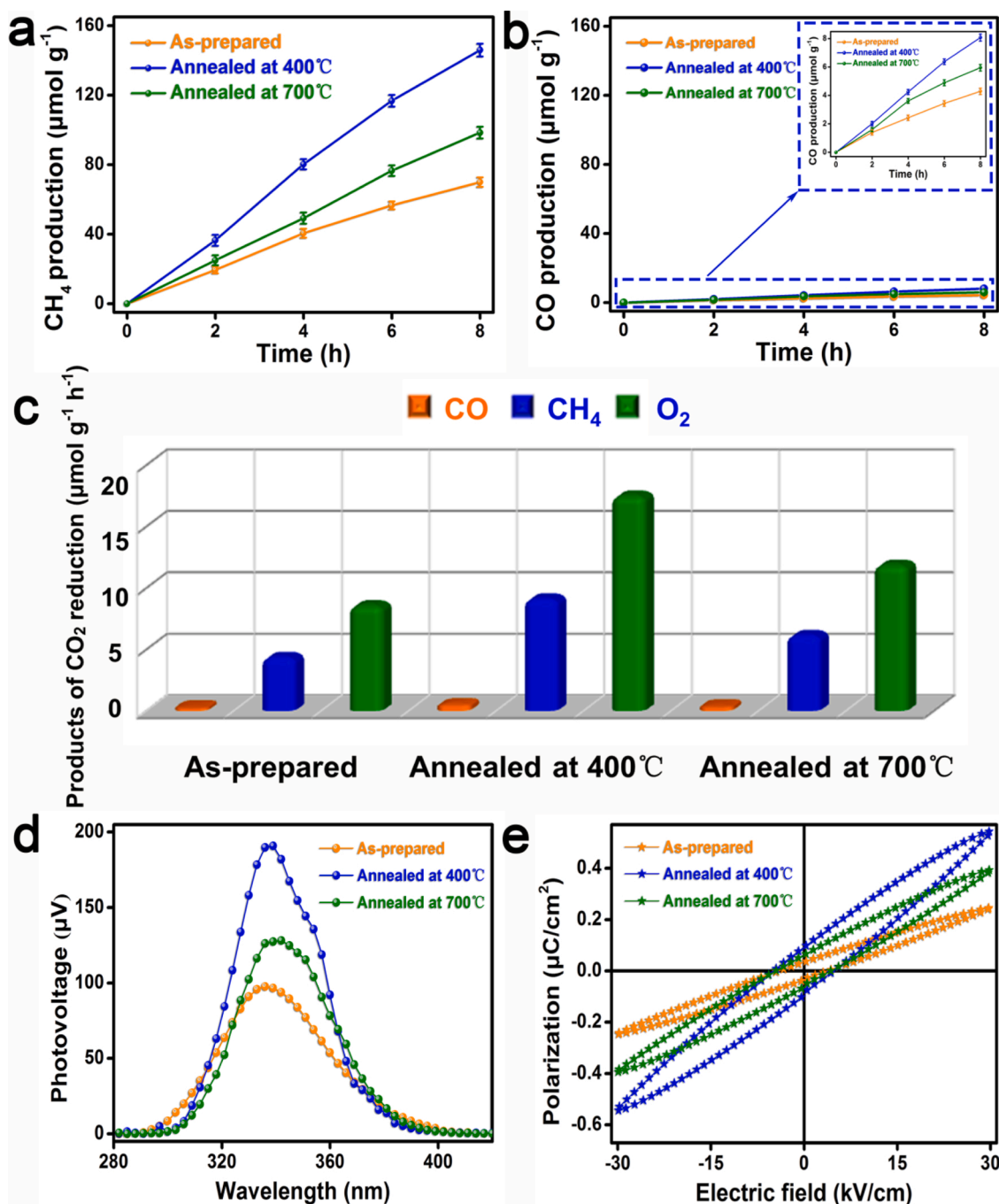
Fig. 6. a-c) Photocatalytic CH_4, CO and O_2 production curves and d) the corresponding CH_4 and CO evolution rates over as-prepared SBN-HR-X kV/cm (X = 5, 10, 20, 30) under simulated solar light. e) PL spectra, f) SPV spectra and g) Photocurrent density of as-prepared SBN-HR-X kV/cm (X = 5, 10, 20, 30) under simulated solar light. h) Schematic illustration for migration of photogenerated electrons and holes promoted by polarization electric field.

comparison with pristine SBN-HR, with SBN-HR-30 kV/cm displaying the lowest peak (Fig. 6e). It means that SBN-HR-30 kV/cm has the most efficient separation efficiency of photoinduced charges. The strongest photovoltage response from surface photovoltage (SPV) spectroscopy and highest photocurrent density are also observed for SBN-HR-30 kV/ cm (Fig. 6f and g), verifying the high charge separation efficiency benefiting from polarization-induced electric field enhancement. The external electric poling causes no significant change in the physical properties of the samples, such as photoabsorption, band energy edges, crystallinity and specific surface area. In contrast, the increase of ferroelectric polarization intensity leads to an stronger in-built electric field and larger band bending to afford a greater potential difference, which

considerably facilitates the charge separation efficiency of ferroelectrics for promoting the photocatalytic CO_2 reduction performance (Fig. 6h). While it is worth noting that the photocatalytic performance will not increase significantly with the increase of the external electric field from 20 to 30 kV/cm. It can be explained as that the domains gradually switch to be aligned to achieve polarization saturation with the increase of poling voltage (Fig. S46). Besides, SBN-HR-30 kV/cm shows more alkaline sites for stronger physisorption and chemisorption of CO_2, which benefits the activation of CO_2 molecules by photoexcited electrons (Fig. S36).

4. Conclusion

In summary, ferroelectric $SrBi_2Nb_2O_9$ nanosheets synthesized by an one-pot hydrothermal route are developed as highly-efficient photocatalysts for CO_2 reduction. Theoretical calculations demonstrated that the photogenerated electrons and holes migrate to the NbO_6 octahedral layers along *c* axis and within the *ab*-plane in the Bi_2O_2 layers, respectively, realizing efficient anisotropic charge migration. Particularly, ferroelectric polarization is uncovered as the decisive factor for the photocatalytic activity by dramatically facilitating charge separation in the bulk phase. Two post-treatments methods, annealing and the electric poling, are revealed to be highly effective approach to improving the ferroelectric polarization of $SrBi_2Nb_2O_9$ nanosheets. The poled post-treatment under the electric field of 30 kV/cm as a deep polarization-enhancement strategy was applied to further promote the ferroelectricity of $SrBi_2Nb_2O_9$ nanosheets, which results in a ~81 times enhancement in CH_4 evolution with a super-high rate of 25.91 μmol g^{-1} h^{-1} and an apparent quantum efficiency (AQE) of 1.96 % at 365 nm, standing among the best photocatalysts reported to date. The findings are expected to underpin future research efforts to develop high-performance materials in other fields, such as electrocatalysis, lithium-ion batteries, supercapacitors.

CRediT authorship contribution statement

Hongjian Yu: Methodology, Software, Writing - original draft. **Hongwei Huang:** Conceptualization, Supervision, Writing - review & editing. **Ali H. Reshak:** Methodology, Software. **Sushil Auluck:** Methodology, Software. **Lizhen Liu:** Data curation. **Tianyi Ma:** Writing - review & editing. **Yihe Zhang:** Supervision.

Declaration of Competing Interest

The authors declare no conflict of interest.

Acknowledgements

Appendix A. Supplementary data

Supplementary material related to this article can be found, in the online version, at doi:https://doi.org/10.1016/j.apcatb.2020.119709.

References

[1] S. Gao, Y. Lin, X.C. Jiao, Y.F. Sun, Q.Q. Luo, W.H. Zhang, D.Q. Li, J.L. Yang, Y. Xie, Nature 529 (2016) 68–71, https://doi.org/10.1038/nature16455.

[2] C. Gao, Q.Q. Meng, K. Zhao, H.J. Yin, D.W. Wang, J. Guo, S.L. Zhao, L. Chang, M. He, Q.X. Li, H.J. Zhao, X.J. Huang, Y. Gao, Z.Y. Tang, Adv. Mater. 28 (2016) 6485–6490, https://doi.org/10.1002/adma.201601387.

[3] H.J. Yu, J.Y. Li, Y.H. Zhang, S.Q. Yang, K.L. Han, F. Dong, T.Y. Ma, H.W. Huang, Angew. Chem. Int. Ed. 58 (2019) 3880–3884, https://doi.org/10.1002/anie.201813967.

[4] L.Q. Ye, X.L. Jin, X.X. Ji, C. Liu, Y.R. Su, H.Q. Xie, C. Liu, Chem. Eng. J. 291 (2016) 39–46, https://doi.org/10.1016/j.cej.2016.01.032.

[5] H.J. Yu, H.W. Huang, K. Xu, W.C. Hao, Y.X. Guo, S.B. Wang, X.L. Shen, S.F. Pan, Y. H. Zhang, ACS Sustain. Chem. Eng. 5 (2017) 10499–10508, https://doi.org/10.1021/acssuschemeng.7b02508.

[6] A. Iwase, S. Yoshino, T. Takayama, Y.H. Ng, R. Amal, A. Kudo, J. Am. Chem. Soc. 138 (2016) 10260–10264, https://doi.org/10.1021/jacs.6b05304.

[7] A. Kubacka, M. Fernandez-Garcia, G. Colon, Chem. Rev. 112 (2012) 1555–1614, https://doi.org/10.1021/cr100454n.

[8] H.W. Huang, S.C. Tu, C. Zeng, T.R. Zhang, A.H. Reshak, Y.H. Zhang, Angew. Chem. Int. Ed. Engl. 56 (2017) 11860–11864, https://doi.org/10.1002/anie.201706549.

[9] L.L. Zhao, Y. Zhang, F.L. Wang, S.C. Hu, X.N. Wang, B.J. Ma, H. Liu, Z. Lin Wang, Y. H. Sang, Nano Energy 39 (2017) 461–469, https://doi.org/10.1016/j.nanoen.2017.07.037.

[10] F. Chen, H.W. Huang, L. Guo, Y.H. Zhang, T.Y. Ma, Angew. Chem. Int. Ed. 58 (2019) 10061–10073, https://doi.org/10.1002/anie.201901361.

[11] J. Li, L.J. Cai, J. Shang, Y. Yu, L.Z. Zhang, Adv. Mater. 28 (2016) 4059–4064, https://doi.org/10.1002/adma.201600301.

[12] F. Chen, Z.Y. Ma, L.Q. Ye, T.Y. Ma, T.R. Zhang, Y.H. Zhang, H.W. Huang, Adv. Mater. 32 (2020), 1908350, https://doi.org/10.1002/adma.201908350.

[13] Z.Y. Jiang, Y.Y. Liu, M.M. Li, T. Jing, B.B. Huang, X.Y. Zhang, X.Y. Qin, Y. Dai, Sci. Rep. 6 (2016), 22727, https://doi.org/10.1038/srep22727.

[14] C. Hu, H. Huang, F. Chen, Y.H. Zhang, Y. Hai, T.Y. Ma, Adv. Funct. Mater. 30 (2020), 1908168, https://doi.org/10.1002/adfm.201908168.

[15] J.J. Shan, F. Raziq, M. Humayun, W. Zhou, Y. Qu, G.F. Wang, Y.D. Li, Appl. Catal. B-Environ. 219 (2017) 10–17, https://doi.org/10.1016/j.apcatb.2017.07.024.

[16] F. Wu, Y.H. Yu, H. Yang, L.N. German, Z.Q. Li, J.G. Chen, W.G. Yang, L. Huang, W. M. Shi, L.J. Wang, X.D. Wang, Adv. Mater. 29 (2017), 1701432, https://doi.org/10.1002/adma.201701432.

[17] W.M. Wu, S.J. Liang, Y. Chen, L.J. Shen, H.R. Zheng, L. Wu, Catal. Commun. 17 (2012) 39–42, https://doi.org/10.1016/j.catcom.2011.10.012.

[18] J.-H. Kim, K.-T. Hwang, U.-S. Kim, Y.-M. Kang, Ceram. Int. 38 (2012) 3901–3906, https://doi.org/10.1016/j.ceramint.2012.01.042.

[19] U.N. Gupta, K. Rao, S. Pradhan, R.K. Jha, H. Muthurajan, H. Ravi, Int. J. Appl. Ceram. Tech. 5 (2010) 101–104, https://doi.org/10.1111/j.1744-7402.2008.02182.x.

[20] B. Zhang, Y.X. Li, J.M. Luo, H. Zhao, J. Zhao, G.H. Dong, Y.Q. Zhu, C.Y. Wang, Appl. Surf. Sci. 391 (2017) 499–506, https://doi.org/10.1016/j.apsusc.2016.06.143.

[21] J. Yang, P.F. Jiang, M.F. Yue, D.F. Yang, R.H. Cong, W.L. Gao, T. Yang, J. Catal. 345 (2017) 236–244, https://doi.org/10.1016/j.jcat.2016.11.007.

[22] T. Wang, X.X. Meng, P. Li, S.X. Ouyang, K. Chang, G.G. Liu, Z.W. Mei, J.H. Ye, Nano Energy 9 (2014) 50–60, https://doi.org/10.1016/j.nanoen.2014.06.027.

[23] J.H. Low, L.Y. Zhang, T. Tong, B.J. Shen, J.G. Yu, J. Catal. 361 (2018) 255–266, https://doi.org/10.1016/j.jcat.2018.03.009.

[24] L. Hao, L. Kang, H.W. Huang, L.Q. Ye, K.L. Han, S.Q. Yang, H.J. Yu, M. Batmunkh, Y.H. Zhang, T.Y. Ma, Adv. Mater. 31 (2019), 1900546, https://doi.org/10.1002/adma.201900546.

[25] H.J. Zhang, L. Liu, Z. Zhou, RSC Adv. 2 (2012) 9224–9229, https://doi.org/10.1039/C2RA20881D.

[26] H.W. Huang, R.R. Cao, S.X. Yu, K. Xu, W.C. Hao, Y.G. Wang, F. Dong, T.R. Zhang, Y.H. Zhang, Appl. Catal. B-Environ. 219 (2017) 526–537, https://doi.org/10.1016/j.apcatb.2017.07.084.

[27] Y.Q. Chen, X.J. Zheng, L. He, X. Feng, Physica Status Solidi A 207 (2009) 1240–1244, https://doi.org/10.1002/pssa.200925490.

[28] X.L. Zhong, J.B. Wang, X.J. Zheng, Y.C. Zhou, G.W. Yang, Appl. Phys. Lett. 85 (2004) 5661–5663, https://doi.org/10.1063/1.1834731.

[29] S.C. Tu, Y.H. Zhang, A.H. Reshak, S. Auluck, S.Q. Ye, T.Y. Ma, H.W. Huang, Nano Energy 56 (2018) 840–850, https://doi.org/10.1016/j.nanoen.2018.12.016.

[30] Y. Zhou, Z. P.Tian, Z.Y. Zhao, Q. Liu, J.H. Kou, X.Y. Chen, J. Gao, S.C. Yan, Z. G. Zou, ACS Appl. Mater. Interfaces 3 (2011) 3594–3601, https://doi.org/10.1021/am2008147.

[31] T. Shaw, M. Mckinstry, P. Mcintry, Rev. Mater. Sci. 30 (2000) 263–298, https://doi.org/10.1146/annurev.matsci.30.1.263.

[32] T. Mihara, H. Yoshimori, H. Watanabe, C. Araujo, J. Appl. Phys. 34 (1995) 5233–5238, https://doi.org/10.1143/JJAP.34.5233.

[33] L.Q. Ye, X.L. Jin, C. Liu, C.H. Ding, H.Q. Xie, K.H. Chu, P.K. Wong, Appl. Catal. B-Environ. 187 (2016) 281–290, https://doi.org/10.1016/j.apcatb.2016.01.044.